

Synchronous reluctance motor with concentrated windings for IE4 efficiency

Original

Synchronous reluctance motor with concentrated windings for IE4 efficiency / Gamba, M., Pellegrino, G., Armando, E., Ferrari, S.. - ELETTRONICO. - (2017), pp. 3905-3912. (Energy Conversion Congress and Exposition (ECCE), 2017 IEEE Cincinnati (USA) 1-5 Oct. 2017) [10.1109/ECCE.2017.8096686].

Availability:

This version is available at: 11583/2694501 since: 2017-12-11T13:18:37Z

Publisher:

IEEE

Published

DOI:10.1109/ECCE.2017.8096686

Terms of use:

This article is made available under terms and conditions as specified in the corresponding bibliographic description in the repository

Publisher copyright

IEEE postprint/Author's Accepted Manuscript

©2017 IEEE. Personal use of this material is permitted. Permission from IEEE must be obtained for all other uses, in any current or future media, including reprinting/republishing this material for advertising or promotional purposes, creating new collecting works, for resale or lists, or reuse of any copyrighted component of this work in other works.

(Article begins on next page)

Synchronous Reluctance Motor with Concentrated Windings for IE4 Efficiency

Matteo Gamba, Gianmario Pellegrino, Eric Armando and Simone Ferrari
Department of Energy

Politecnico di Torino, 10129 Turin, Italy

Email: matteo.gamba@polito.it, gianmario.pellegrino@polito.it, eric.armando@polito.it, simone.ferrari@polito.it

Abstract—This paper investigates the applicability of fractional-slot concentrated windings to Synchronous Reluctance Motors for industry applications. Tooth-wound winding arrangements are attractive for the industry due to their lower cost of manufacturing, but when associated to a synchronous reluctance rotor they tend to lower the output torque and power factor of the machine significantly, and to excite high values of torque ripple. The proposed analysis shows that after design optimization one synchronous reluctance machine with concentrated windings can reach the IE4 (super-premium) efficiency class within the same frame of a distributed-winding synchronous reluctance machine of the same size. Moreover, the paper demonstrates that the synchronous reluctance rotor must be purposely redesigned for the new stator, when passing from distributed to concentrated windings, for the sake of torque ripple mitigation. A step by step design procedure is provided, supported by finite-element analysis and experimental results.

I. INTRODUCTION

The winding topologies adopted for three phase AC machines can be classified as [1]:

- distributed windings, with overlapped end turns [2];
- concentrated windings, with non-overlapped end turns, also called tooth-wound windings.

Traditionally, the Synchronous Reluctance (SyR) machine is based on distributed windings, identical to those in use for squirrel-cage induction motors [3], [4]. Concentrated windings have become attractive in the last fifteen years for their simple manufacturing and for the reduction of the end-winding length with benefits of reduced copper loss and reduced axial length of the machine. Machines with concentrated-winding stators are also called fractional-slot machines, because tooth-wound, concentrated coils are always associated to a fractional number of slots per pole per phase, smaller than one.

Although the design of SyR motors with distributed windings is a widely explored topic in literature, the case of concentrated-winding SyR motors is way less explored. The main disadvantage related to the CW-SyR solution is the strong reduction of the machine reluctance, with significant reduction of output torque and power factor. Moreover, torque ripple tends to be higher than in the distributed-winding case. The paper [2] reports a comparison between distributed and concentrated winding solutions, for a SyR machine with permanent magnet assistance, showing that the reluctance torque contribution is dramatically reduced when passing from distributed to concentrated windings, using the same

rotor. Nevertheless, another work [5] shows that adopting a modular stator construction in a CW-SyR machine the slot fill factor equals 0.7, with benefits on torque density and efficiency. Based on this background, this paper proposes the design of a CW-SyR machine capable of overcoming the IE4 efficiency target, intended as an alternative solution of simpler manufacturing for variable speed drives in industry applications.

The paper presents a preliminary design stage, where the optimal pole number is selected considering efficiency and thermal aspects. Then, a multi-objective optimization procedure is applied to refine the design of the rotor and stator geometry, in order to maximize the output torque and minimize the torque ripple. A sensitivity investigation of the effect of the number of rotor barriers on the torque ripple is presented, and a novel solution with minimized torque ripple amplitude is proposed. Finite-element analysis and design optimization are performed using open source resources [16] and [15]. A prototype was built and tested in order to validate the results of the proposed analysis.

II. PRELIMINARY DESIGN

A. Sizing

The machine was designed according to specifications reported in Tab I. The benchmark is a self-ventilated three-phase SyR motor rated 7.5 kW at 1500 rpm, with three slots per pole per phase ($q = 3$). The reference machine is a high efficiency machine, well above the IE4 class. The geometry of this topology is qualitatively represented in Fig 1a. Data reported in Tab I, such as the airgap diameter, the outer stator diameter, the stack length and the airgap length are kept constant also for the CW-SyR prototype under design, for simplifying the comparison between the two motors.

B. Slot-Pole Combination

The proposed three-phase machine has concentrated windings with one coil per tooth, as represented in Fig 1b. Feasible concentrated-winding configurations are well summarized in [7]. Among the combinations with a winding factor greater than 0,8, the solution with $q = 1/2$ is the one that presents the highest compatibility with the reluctance rotor, as shown in the analysis [5] and [6]. The winding factor is $k_w = 0,866$ and this configuration is compatible with any number of pole-pairs, giving a certain degree of flexibility to the designer.

TABLE I
MACHINE SPECIFICATION

Stator outer diameter [mm]	100
Rotor outer diameter [mm]	65
Airgap length [mm]	0.5
Stack length [mm]	215
Number of series turns per phase N_s	87
Nominal Power [kW]	7.5
Nominal Speed [rpm]	1500
Maximum Speed [rpm]	5000
Nominal phase voltage [V] pk	310
Nominal phase current [A] pk	45
Nominal Joule Loss [W]	270

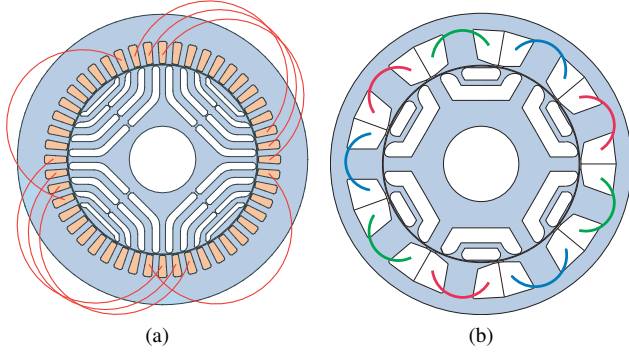


Fig. 1. Cross section of a) $q = 3$ benchmark b) $q = 1/2$ CW-SyR motor under investigation

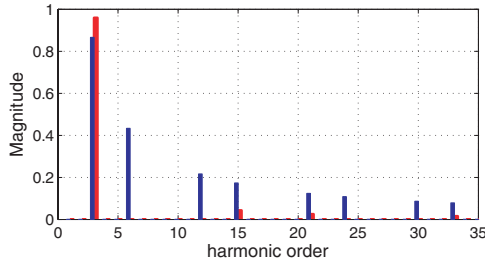


Fig. 2. Winding factor and MMF spatial harmonics of $q=1/2$ (blue bars) and $q=3$ (red bars)

The slot/pole combinations typical of this configuration are $3/2$, $6/4$, $9/6$ et cetera. As a counter example, combinations such as $q = 2/5$ or $q = 2/7$ are incompatible with pole-pair numbers non multiple of five or seven, respectively.

The magneto-motive force (MMF) spectrum of a three-phase winding with $q = 1/2$ is reported in Fig. 2, compared to the one of the benchmark machine. The MMF spectrum contains both even and odd harmonics, as a consequence of the non anti periodic symmetry of the airgap MMF distribution over two pole pitches. On the contrary, the distributed winding configuration used for comparison contains only odd harmonics (red bars). The harmonic content of the $q = 1/2$ winding results in torque harmonics (i.e. torque ripple) and potential iron loss.

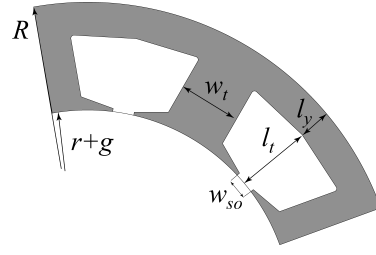


Fig. 3. stator cross section main parameters

C. Preliminary Design of tooth width and yoke length

The design of CW-SyR motor is not straightforward. For this paper, an optimization algorithm will design both stator and rotor of the final machine, but for the preliminary design, the machine is designed using the equation for distributed winding stator. Fig 3 shows the main parameters of the stator: the tooth width w_t and the yoke length l_y , that can be expressed by (1) and (2).

$$w_t = b \frac{\pi r}{3pq} \quad (1)$$

$$l_y = \frac{3}{\pi} q w_t \quad (2)$$

Where b is the ratio between the peak airgap induction and the steel induction (3). In the preliminary design stage, a balanced machine is used, then $b = 0.5$.

$$b = \frac{B_{gap}}{B_{Fe}} \quad (3)$$

D. End Winding Length

The use of tooth-wound configurations permits a consistent reduction of the end winding length l_{end} . End winding represents non active copper mass, unnecessary for torque production, their reduction reduce the copper mass, and also the total axial length of the machine at constant stack length. The l_{end} for overlapped winding (Fig 4a,b) could be analytically estimated with (4).

$$l_{end} = 2l_t + \left(r + \frac{l_t}{2} \right) \alpha \quad (4)$$

Where l_t is the tooth length, r is the airgap rotor radius and $\alpha = \pi/p$ is the pole span.

A second formula (5) according to Fig 4c,d is used for concentrated winding:

$$l_{end} = \frac{1}{2} \left[w_t + \pi \left(r + \frac{l_t}{2} \right) \sin \left(\frac{\alpha_{slot}}{2} \right) \right] \quad (5)$$

Where w_t represents the tooth width and α_{slot} is the slot angle defined as $\alpha_{slot} = \frac{\pi}{3pq}$. Considering the designed machines reported in Fig 1 whose main data are shown in Tab I, according to (4) for $q=3$ motor $l_{end} = 146 \text{ mm}$, using (5), for $q = 1/2$, $l_{end} = 51 \text{ mm}$ (35% of the $q = 3$). Even if the number of poles are different it will be shown in the following that also using the same number of poles the tooth coil presents a reduction of 50% in end winding length.

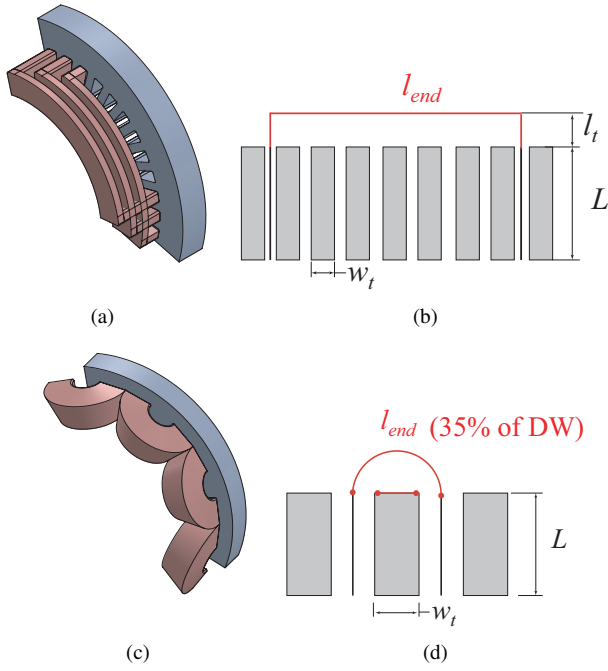


Fig. 4. a) 3D view of the end winding connection according to (4); b) upper view of $q=3$; c) 3D view of $q=1/2$ end winding connection; d) upper view of $q=1/2$

E. Optimal number of poles

The number of pole pairs must be preliminary choose. The approach used here is to use a simplified design procedure in order to find the optimal number of poles that minimizes losses in the machine. The general torque equation is:

$$T = \frac{3}{2} p \left(\frac{\xi - 1}{\xi} \right) L_{md} I^2 \frac{\sin(2\gamma)}{2} \quad (6)$$

L_{md} is the magnetizing inductance express by:

$$L_{md} = \frac{6}{\pi} \frac{r}{g} \mu_0 L \frac{\left(k_w N_s \right)^2}{p^2} \quad (7)$$

where ξ is the anisotropy ratio $\xi = L_{md}/L_{mq}$, γ is the current phase angle. Writing the Joule losses as a function of torque, equation (8) is obtained.

$$P_{js} = T \frac{4\pi}{\mu_0} \frac{g}{r} \frac{\xi}{\xi - 1} k_w^2 \sin(2\gamma) \rho \frac{p K_{end}}{K_{cu} A_s} \quad (8)$$

K_{end} is the end winding factor and A_s is the total slots surface.

$$K_{end} = \frac{L + l_{end}}{L} \quad (9)$$

$$A_s = \pi l_t (2R - l_y - l_t) - 6pq w_t l_t = B + \frac{A}{p} \quad (10)$$

$$A = \frac{(b\pi r)^2}{3pq} - \frac{\pi^2 br}{3pq} \left(\frac{R + r}{2} \right) \quad (11)$$

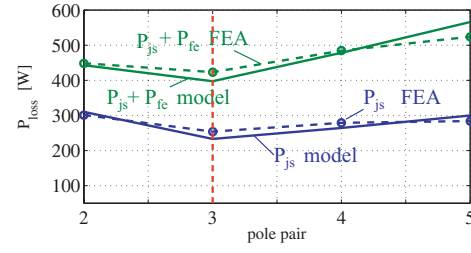


Fig. 5. Losses function of pole pair, the output torque is constant and equal to 50Nm @ 1500rpm

$$B = 2b\pi (r^2 - rR) + \pi(R^2 - r^2) \quad (12)$$

Substituting (5) in (9), it is possible to obtain the end winding factor function of the pole pair as (13):

$$K_{end} = 1 + \frac{1}{2L} \left(\frac{C}{p} - \frac{D}{p^2} \right) \quad (13)$$

where

$$C = \frac{\pi}{3qL} \left(br + \pi \left(\frac{r+R}{4} \right) \right) \quad (14)$$

$$D = \frac{br}{2L} \left(\frac{\pi}{6q} \right)^2 \quad (15)$$

Substituting (10) and (13) in (8) and deriving, the pole pair that minimizes losses could be calculate according to (16).

$$\begin{aligned} \frac{\partial P_{js}}{\partial p} \Big|_{T=50Nm} &= 0 \rightarrow \\ \rightarrow p_{opt} &= \frac{1}{2B} \left(\sqrt{2(2A^2 - CAB - DB^2)} - 2A \right) \end{aligned} \quad (16)$$

Fig 5 reports the results of previous formulation compared to FEA results. The results are equivalent, the discrepancies is related to inaccuracies in the anisotropy factor ξ and the magnetization inductance L_{md} models. Considering only Joule losses, solution at $p = 3$ is the best one, introducing the iron losses (green line in Fig 5), the discrepancy between $p = 2$ and $p = 3$ become lower but three pole pairs remain the solution at minimum losses.

F. Simplified Thermal Model

Based on [9] authors implement a simplified thermal network suitable for the estimation of the copper over-temperature respect to the frame temperature. In [10] are summarized many problem in the estimation of the correct heat flow in electrical machine. The model compute the over-temperature in steady state condition for this reason thermal capacity are neglected. The following hypothesis have been assumed:

- Frame temperature is assumed constant and imposed as a parameter.
- Only stator joule losses are considered.
- Only radial heat transfer is considered, no 3D effects are taken into account. End winding connection are

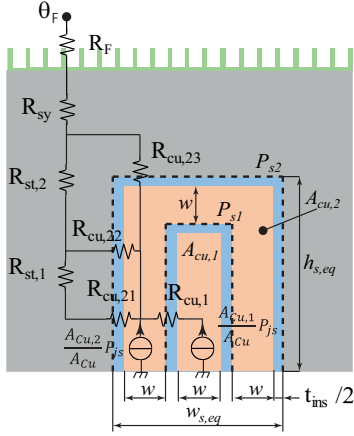


Fig. 6. Thermal network

considered only in Joule losses computation, but not in heat network.

Fig 6 reports the equivalent circuit model, representative of all the machine. The slot cross-section is divided in two portions: an inner area, $A_{cu,1}$, and an outer area $A_{cu,2}$. The Joule loss production is proportional to the area.

With reference to Fig 6, stator yoke thermal resistance can be expressed by (17):

$$R_{sy} = \frac{1}{2\pi\lambda_{fe}L} \left(\frac{R}{r+g+l_t} \right) \quad (17)$$

The tooth resistance is divided into two components, one, $R_{st,1}$, representing temperature drop at the middle of the tooth, and second one, $R_{st,2}$, representing the drop between the middle and the end of the tooth.

$$R_{st,1} = \frac{1}{2\pi\lambda_{fe}k_{pth}L} \left(\frac{r+g+l_t/2}{r+g} \right) \quad (18)$$

$$R_{st,2} = \frac{1}{2\pi\lambda_{fe}k_{pth}L} \left(\frac{R}{r+g+l_t/2} \right) \quad (19)$$

Where λ_{fe} is the iron thermal coefficient generally equal to 25W/(mK); k_{pth} represents the ratio between the iron volume and total volume (iron+slot) without the yoke.

The total insulation thickness in the slot is assumed:

$$t_{ins} = \frac{(1-k_{cu})A_{slot}}{P_s} \quad (20)$$

Where A_{slot} is the stator slot surface, P_s is the external slot perimeters, see Fig 6. The insulation thickness is assumed divided into two portion with equal thickness $t_{ins,1} = t_{ins,2} = t_{ins}/2$. The thermal resistance of the insulation layers are:

$$R_{cu,1} = \frac{t_{ins,1}}{P_{s,1}\lambda_{ins}L} \frac{1}{6pq} \quad (21)$$

$$R_{cu,21} = R_{cu,22} = \frac{1}{2} \frac{t_{ins,2}}{2l_t\lambda_{ins}L} \frac{1}{6pq} \quad (22)$$

Where $\lambda_{ins} = 0,3$ is an equivalent insulation coefficient that take into account the use of thermal resins in the slots.

TABLE II
TEMPERATURE VARIATION AT DIFFERENT POLE PAIRS

q	p	$R_s(20^\circ C)$ [Ω]	$P_{j,s}(20^\circ C)$ [W]	$\Delta\theta$ [$^\circ C$]
3	2	0,348 ($k_{cu} = 0,44$)	300	7
1/2	2	0,164 ($k_{cu} = 0,6$)	301,35	40
1/2	3	0,106 ($k_{cu} = 0,6$)	241,84	20
1/2	4	0,09 ($k_{cu} = 0,6$)	279	16,5
1/2	5	0,079 ($k_{cu} = 0,6$)	284	13,5

The end of the slot is modeled by a single resistance directly connected to the yoke.

$$R_{cu,23} = \frac{t_{ins,2}}{2w_{s,eq}\lambda_{ins}L} \frac{1}{6pq} \quad (23)$$

The frame resistance R_F can be expressed as:

$$R_F = \frac{1}{\pi k_c L R} \quad (24)$$

Where $k_c = 10^3$ is the frame-core contact coefficient [11].

Solving the network shown in Fig 6, it is possible to calculate the winding temperature. The frame temperature is assumed constant and equal to $70^\circ C$, that represents an experimental verified temperature for IE4 motor. In Tab II are summarized the over-temperature for the distributed and fractional slot winding solutions, it is evident that passing from $p = 2$ to $p = 3$ the over-temperature is reduced of one half. The reduction, increasing the number of poles, become lower and lower. The choice of $p = 3$ represents a good trade off between copper over-temperature and efficiency results.

III. DESIGN OPTIMIZATION

The optimization of the machine geometry is performed to obtain the best tradeoff between torque production and torque ripple [8]. Tab I shows the main geometric parameters, that will be constant during the optimization process. Tab III shows the input variables that will be optimized and their boundaries during the optimization process, with the normalized format used in [15]. $\Delta\alpha$, h_c and Δx define the rotor geometry, as addressed later; w_t , l_t and w_{so} describe the stator geometry, according to Fig 3; γ is the current phase angle in the dq frame. The optimization process is based on a genetic algorithm. For each candidate machine, a set of optimization variables is randomly chose, and then, the machine is evaluated using Finite-Elements analysis in terms of mean torque and torque ripple, at constant Joule loss $P_{j,s} = 320W$, that is the same of the $q = 3$ motor in overload condition (120%).

A. Modelling of the rotor barriers

The rotor geometry heavily affects the performance of the SyR machine. Torque, torque ripple and losses are essentially determined by the flux barrier shapes, sizes and positions [8]. The key rotor parameters to define a multi barrier rotor are the number of flux barriers n_{lay} , the angular position of their ends at the airgap ($\Delta\alpha$), the thicknesses of the flux barriers (h_c) and the offset of the flux barriers (Δx). The first parameter

TABLE III
OPTIMIZE VARIABLES

variable		Constraint	
		min	max
$\Delta \alpha$	[pu]	0.13	0.5
Δh_c	[pu]	0.2	1.0
Δx	[pu]	-0.5	0.5
l_t	[mm]	17	23
w_t	[mm]	18	31
w_{so}	[pu]	0.1	0.5
γ	[°el]	40	70

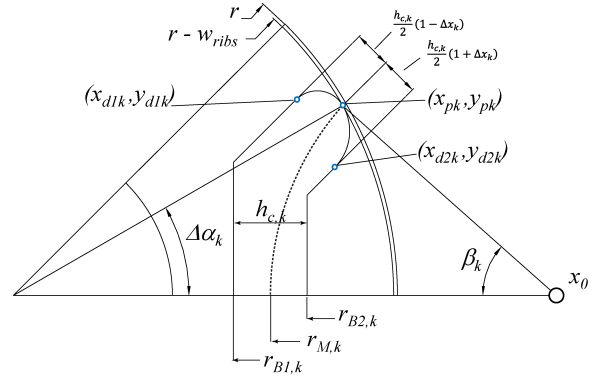


Fig. 7. Rotor barrier construction details

is a scalar number while the other ones are vector of n_{lay} elements. The first barrier is defined as the outer one (so the closest one to the airgap). Different geometries were presented over the years [4], [8] and [12] where is shown that a minimum number of parameters per barrier is three. The geometry used in this paper, named Segment geometry, presents three degree of freedom and a shape suitable for the insertions of permanent magnets. The design procedure is detailed in the following, with reference at Fig 7.

- 1) Calculation of x_0 by (25) as (25).

$$x_0 = \frac{r}{\cos\left(\frac{\pi}{2p}\right)} \quad (25)$$

- 2) The optimization process randomly choose the $h_{c,k}$ and $\Delta\alpha_k$ value.
- 3) From $\Delta\alpha_k$, calculation of $r_{M,k}$ by (26) obtaining the arc profile illustrated in Fig 7, and then, the points $(x_{p,k}, y_{p,k})$, which are the extreme points of the flux barrier near the airgap.

$$\beta_k = \arctan\left(\frac{r \sin(\alpha_k)}{x_0 - r \cos(\alpha_k)}\right) \quad (26)$$

$$r_{M,k} = \frac{x_0 - r \cos(\alpha_k)}{\cos(\beta_k)} \quad (27)$$

$$x_{p,k} = \frac{(r - w_{rib})^2 - r_{\beta,k}^2 + x_0^2}{2x_0^2} \quad (28)$$

$$y_{p,k} = \sqrt{\frac{(r - w_{rib})^2 (2x_0 - 1) + r_{M,k}^2 - x_0^2}{2x_0}} \quad (29)$$

- 4) Calculation of $r_{B1,k}$ and $r_{B2,k}$, which define the vertical sided of the flux barriers, according to $h_{c,k}$ (barrier width) and Δx_k (offset respect to initial medium point $r_{M,k}$).

$$r_{B1,k} = r_{M,k} + \frac{h_{c,k}}{2} (1 - \Delta x_k) \quad (30)$$

$$r_{B2,k} = r_{M,k} - \frac{h_{c,k}}{2} (1 + \Delta x_k) \quad (31)$$

- 5) Calculation of the upper ($j = 1$) and lower ($j = 2$) lines which define the upper and lower sides of the flux barriers using (32).

$$y = \tan\left(\frac{\pi}{2p}\right) x + \left(\frac{B}{2} - \sqrt{\frac{B^2}{4} - C_j}\right) \quad (32)$$

Where

$$B = x_{p,k} - \tan\left(\frac{\pi}{2p}\right) x_{p,k} \quad (33)$$

$$C_1 = y_{p,k}^2 + \tan^2\left(\frac{\pi}{2p}\right) x_{p,k}^2 - 2 \tan\left(\frac{\pi}{2p}\right) x_{p,k} y_{p,k} + \left(\frac{h_{c,k}}{2} (1 - \Delta x)\right)^2 \left(1 + \tan^2\left(\frac{\pi}{2p}\right)\right) \quad (34)$$

$$C_2 = y_{p,k}^2 + \tan^2\left(\frac{\pi}{2p}\right) x_{p,k}^2 - 2 \tan\left(\frac{\pi}{2p}\right) x_{p,k} y_{p,k} + \left(\frac{h_{c,k}}{2} (1 + \Delta x)\right)^2 \left(1 + \tan^2\left(\frac{\pi}{2p}\right)\right) \quad (35)$$

- 6) Finally the coordinate $(x_{d1,k}, y_{d1,k})$ $(x_{d2,k}, y_{d2,k})$ are obtained evaluating the circumference tangent to the upper and lower sides of the barriers and passing for $(x_{p,k}, y_{p,k})$ evaluated in (28) and (29).

B. Results: the Armchair Solution

The optimization process was executed using an Intel i7 3.20GHz and 16 GB of RAM, with 10000 functional calls and four repetition of the optimization procedure. A sensitivity analysis is carried out varying the number of flux barriers. In Fig 8a the Pareto Fronts summarize the results: it is clear that solutions with 3 and 4 flux barriers are not able to produce a consistent reduction of the torque ripple. The two flux barrier solution presents two different front, one with similar ripple to the other cases, and one where is present the selected machine with ripple comparable to the distributed winding motor. In Fig 8b, are shown the torque ripple profile for the benchmark ($q = 3$) the selected low ripple solution ($q=1/2$ Armchair) and a 3 and 4 layer solutions at $P_j = 320W$. It is evident that the

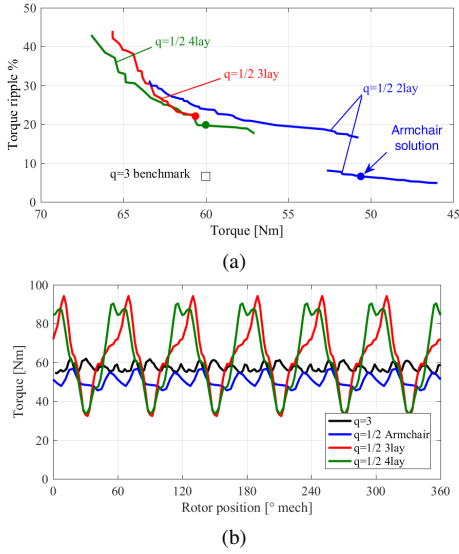


Fig. 8. a)Pareto Front of different repetitions of the optimization process, b) torque ripple of the benchmark machine and the results from optimization process

TABLE IV
ARMCHAIR DATA

variable	value
$\Delta \alpha$	[°] [9; 14]
h_c	[mm] [8.2; 9.8]
Δx	[pu] [0; 0.39]
w_t	[mm] 20
l_t	[mm] 10.3
w_{so}	[pu] 0.15

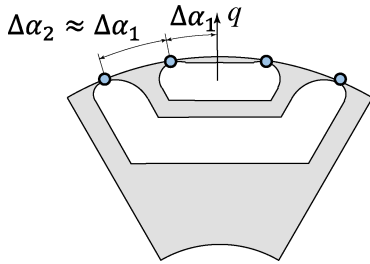


Fig. 9. Armchair Solution

ripple exhibited by the machine with more than 2 layers is not acceptable for common application.

Fig 1b show the geometry of the selected low ripple solution, and Fig 9 shows in detail the rotor geometry. This design presents a thin flux guide between the two flux barrier, the position of the flux barrier at the airgap is quite regular, and an equivalent number of rotor slots per pole pairs could be defined: $n_r = 8$, the equivalent n_r are represented in Fig 9, by blue dot on the periphery of the rotor. Tab IV reports a summary of the main geometric data of this machine. The stator of the selected machine presents $b = 0.44$ and $l_y = 0.5w_t$ while, a balanced machine (as defined in Section II.C) with this slot/pole combination has $b = 0.5$ and $l_y \simeq 0.48w_t$. This fact validate the preliminary design equations.

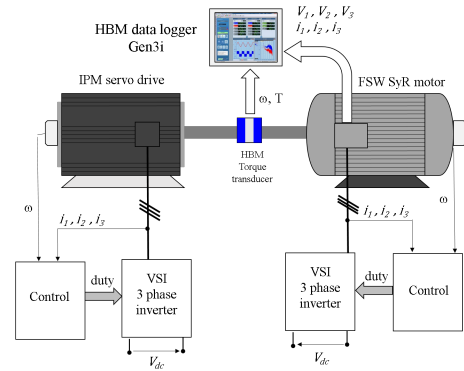


Fig. 10. Test bed setup

IV. EXPERIMENTAL RESULTS

A. Test Bed Description

The test rig for the experimental validation is shown in Fig 10. The Motor under test (MUT) is supplied by an IGBT three phase inverter controlled with dSpace board 1103. The MUT is shaft connected to a Driving Machine (DM) which set the speed during the tests. A HBM Gen 3i [17] records the measures of currents and voltages applied to the MUT and torque and speed at the shaft connection. The sample frequency is set to 2MSamples/s.

The test procedure is composed by three steps, described in the following.

- 1) **Magnetic Model Identification:** The purpose of this test is to obtain the flux linkage maps in the $i_d - i_q$ plane. The test procedure is explained in [13]. During this test, MUT is current controlled over a regular grid in $i_d - i_q$ plane, and the DM set the speed at 500 rpm (one third of the rated one).
- 2) **Torque Ripple Identification:** The purpose of this test is to obtain the torque ripple maps in the $i_d - i_q$ plane. The test procedure is similar to the previous, but the speed is very low (10 rpm) in order to have a good resolution of the torque in the mechanical period. A gearbox is mounted between the torque meter and the DM in order to filter the torque ripple of the DM and help it to keep the speed constant.
- 3) **Efficiency measurement:** The purpose of this test is to measure the machine efficiency. MUT is torque controlled and DM keep the speed constant at the rated one.

B. Flux and Torque Maps

The flux behavior of the machine is shown in Fig 12, finite element and experimental results presents a good match along the d-axis, instead FEA flux curve along the q-axis are lower than the experimental one. The difference is give by the fringing effect, explained in [14], which is not correctly evaluated with 2D FEA. Experiments shows that the machine presents low anisotropy, and this badly affect the torque production shown in Fig 12b. The MTPA presents an angle close to $45^\circ el$. The wrong estimation of the q-axis inductance



Fig. 11. Photo of test bed for magnetic model identification and efficiency measure

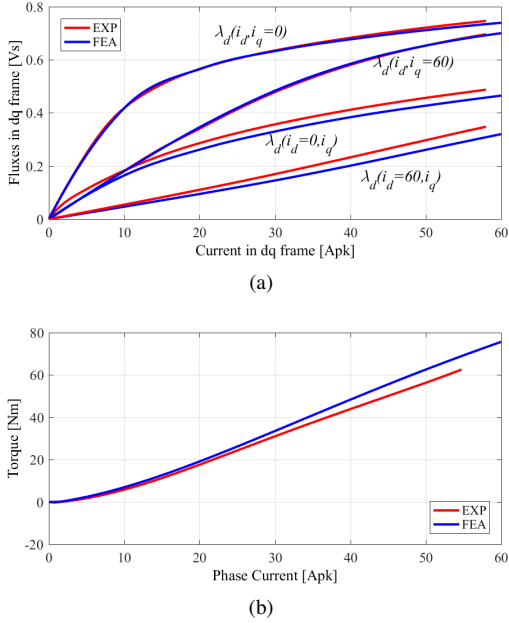


Fig. 12. a) Flux and current in dq reference frame; b) Torque versus Peak Current along the MTPA trajectory

leads to an error of about 10% on the rated torque of the machine.

C. Torque Ripple profile

Fig 13 shows the torque ripple contour in the dq plane. A minimum of the torque ripple exist along the MTPA. FEA and experimental torque results presents a good match, but they differ in mean value. This is related to the higher q-axis flux shown in Fig 12. Reduction of the d-axis component and increment of q-axis current leads to higher increment in torque ripple, this effect is evidenced in Fig 14, that shows the torque profile for three points with same current amplitude, but different current angle.

Another representation of the torque ripple varying with current angle is shown in Fig 15; by this charts is evident that at higher current angle the ripple increase; on the other hand current angle over $60^\circ el$ does not represent a real working point, for this machines, this is related to the lower anisotropy of this motor and the fact that they do not present a constant power profile. A minimum of the torque ripple in the FEA

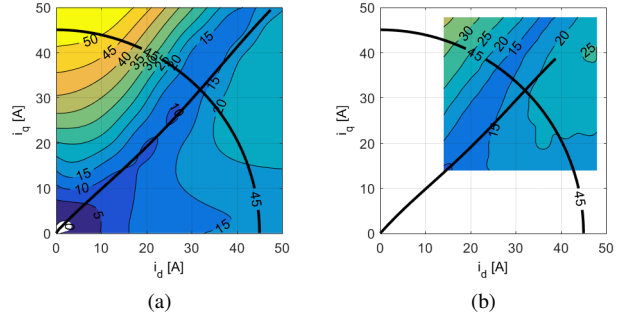


Fig. 13. Torque ripple contour in $i_d i_q$ reference frame: a) FEA results, b) experimental results

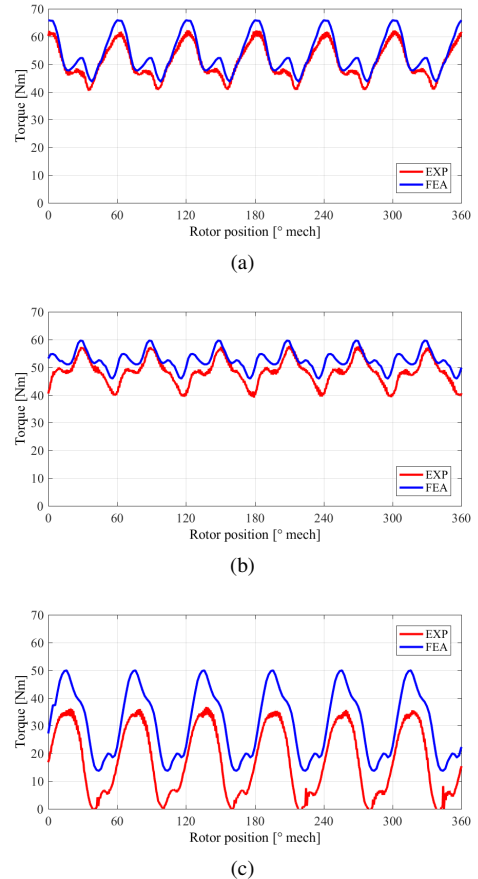


Fig. 14. Torque ripple, a) 45A $35^\circ el$, b) 45A $45^\circ el$, c) 45A $65^\circ el$

results is obtained at the maximum torque (along the MTPA), and experimental results confirm this trend.

D. Efficiency

The measured efficiency is illustrated in Fig 16. Black dots are the measured points and blue line is FEA results. At the nominal power, the efficiency results lower than IE4 target. The efficiency of the designed machine is compared with the benchmark and an induction motor solution with same ratings: the CW-SyR is in the middle of this two solutions. Usually, in fans and pumps applications, machine works like in Fig 16:

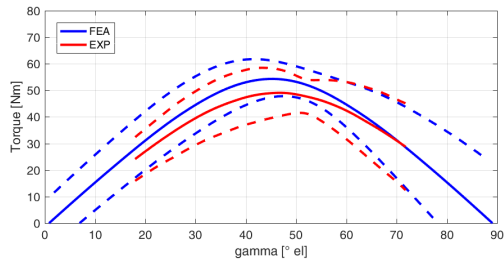


Fig. 15. Mean torque and torque ripple at imposed current value, varying the current angle $i_d i_q$ reference frame

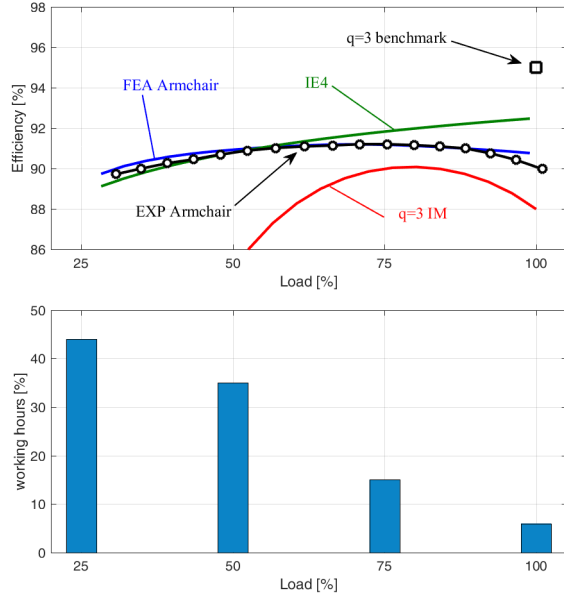


Fig. 16. Efficiency vs output torque at constant speed imposed to 1500rpm

for 44% of their life at 25% of the rated power, where IE4 class is reached. The efficiency measured on the prototyped machine is penalized also by the low slot fill factor (equal to $k_{Cu} = 0,45$) due to some manufacturing problems. Admitting an improvement of the fill factor up to value of $k_{Cu} = 0,6$ is possible to obtain efficiency higher than 92% @ 7,5kW, reaching the IE4 efficiency target.

V. CONCLUSION

This paper presents the design of a 9 slots - 6 poles synchronous reluctance machine prototype intended for IE4 efficiency class in industrial application. The designed machine is easy to manufacture at low cost. The rotor design procedure is explained in details, and it is purposely optimized in order to minimize the torque ripple. The experiments confirm the low torque ripple in the designated conditions of Maximum Torque per Ampere. Tests also show that is nearly possible to reach the IE4 level, even with concentrated windings. Open issues are the poor power factor and the higher copper overtemperature, if compared with distributed winding solution.

REFERENCES

- [1] A. M. EL-Refai, "Fractional-Slot Concentrated-Windings Synchronous Permanent Magnet Machines: Opportunities and Challenges," in IEEE Transactions on Industrial Electronics, vol. 57, no. 1, pp. 107-121, Jan. 2010. doi: 10.1109/TIE.2009.2030211.
- [2] M. Gamba, G. Pellegrino and A. Vagati, "A new PM-assisted Synchronous Reluctance machine with a nonconventional fractional slot per pole combination," 2014 International Conference on Optimization of Electrical and Electronic Equipment (OPTIM), Bran, 2014, pp. 268-275.
- [3] Pellegrino G., Guglielmi P., Vagati A., and Villata F., "Core losses and torque ripple in ipm machines: Dedicated modeling and design tradeoff," Industry Applications, IEEE Transactions on, vol. 46, no. 6, pp. 2381-2391, Nov-Dec 2010.
- [4] Vagati A., Pastorelli M., Francheschini G. and Petrache S. C., "Design of low-torque-ripple synchronous reluctance motors," in IEEE Transactions on Industry Applications, vol. 34, no. 4, pp. 758-765, Jul/Aug 1998.
- [5] C. M. Spargo, B. C. Mecrow, J. D. Widmer, C. Morton and N. J. Baker, "Design and Validation of a Synchronous Reluctance Motor With Single Tooth Windings," in IEEE Transactions on Energy Conversion, vol. 30, no. 2, pp. 795-805, June 2015.
- [6] J. M. Park, S. I. Kim, J. P. Hong and J. H. Lee, "Rotor Design on Torque Ripple Reduction for a Synchronous Reluctance Motor With Concentrated Winding Using Response Surface Methodology," in IEEE Transactions on Magnetics, vol. 42, no. 10, pp. 3479-3481, Oct. 2006.
- [7] J. Cros and P. Viarouge, "Synthesis of high performance PM motors with concentrated windings," IEEE Trans. Energy Convers., vol. 17, no. 2, pp. 248-253, Jun. 2002.
- [8] Cupertino, F.; Pellegrino, G.; Gerada, C., "Design of Synchronous Reluctance Motors With Multiobjective Optimization Algorithms," Industry Applications, IEEE Transactions on, vol. 50, no. 6, pp. 3617-3627, Nov-Dec. 2014.
- [9] A. Boglietti, A. Cavagnino, M. Lazzari and M. Pastorelli, "A simplified thermal model for variable-speed self-cooled industrial induction motor," in IEEE Transactions on Industry Applications, vol. 39, no. 4, pp. 945-952, July-Aug. 2003.
- [10] D. Staton, A. Boglietti and A. Cavagnino, "Solving the More Difficult Aspects of Electric Motor Thermal Analysis in Small and Medium Size Industrial Induction Motors," in IEEE Transactions on Energy Conversion, vol. 20, no. 3, pp. 620-628, Sept. 2005.
- [11] P. H. Mellor, D. Roberts and D. R. Turner, "Lumped parameter thermal model for electrical machines of TEFC design," in IEE Proceedings B - Electric Power Applications, vol. 138, no. 5, pp. 205-218, Sept. 1991.
- [12] M. Gamba, G. Pellegrino and F. Cupertino, "Optimal number of rotor parameters for the automatic design of Synchronous Reluctance machines," 2014 International Conference on Electrical Machines (ICEM), Berlin, 2014, pp. 1334-1340.
- [13] E. Armando, R. I. Bojoi, P. Guglielmi, G. Pellegrino and M. Pastorelli, "Experimental Identification of the Magnetic Model of Synchronous Machines," in IEEE Transactions on Industry Applications, vol. 49, no. 5, pp. 2116-2125, Sept.-Oct. 2013.
- [14] M. Gamba, G. Pellegrino, A. Cavagnino, Z. Gmyrek and M. Lefik, "Rotor End Effects on FEM-based Flux Mapping of Synchronous Reluctance Motors," 2017 IEEE International Electric Machines and Drives Conference (IEMDC), Miami, FL, 2017
- [15] Cupertino F. et al., "Syre - Synchronous Reluctance (machines) evolution" [Online]. Available: <http://sourceforge.net/projects/syr-e/> [Accessed: 10- Nov- 2015].
- [16] Meeker D., "Finite Element Method Magnetics (FEMM)". [Online]. Available: <http://femm.foster-miller.net> [Accessed: 10- Nov- 2015]
- [17] <https://www.hbm.com/en/3868/data-recorder-gen3i-and-transient-recorder/>. [Accessed: 01- June- 2016]